Hybridization of battery with pico hydel for frequency regulation of microgrids using synchronverter control

Vasudevan, Krishnakumar R.; Ramachandaramurthy, Vigna K.; Venugopal, Gomathi; Guerrero, Josep M.

[Link to publication from Aalborg University](#)

The Institution of Engineering and Technology WILEY

ORIGINAL RESEARCH PAPER

Hybridization of battery with pico hydel for frequency regulation of microgrids using synchronverter control

Krishnakumar R. Vasudevan[1] | **Vigna K. Ramachandaramurthy[1]** | **Gomathi Venugopal[2]** |
Josep M. Guerrero[3]

[1] Institute of Power Engineering, Department of Electrical Power Engineering, College of Engineering, Universiti Tenaga Nasional, Jalan IKRAM-UNITEN, Kajang, Selangor 43000, Malaysia

[2] Department of Electrical and Electronics Engineering, Anna University, Chennai 600025, India

[3] Department of Energy Technology, Aalborg University, Aalborg 9220, Denmark

Correspondence
Vigna K. Ramachandaramurthy, Institute of Power Engineering, Department of Electrical Power Engineering, College of Engineering, Universiti Tenaga Nasional, Jalan IKRAM-UNITEN, 43000 Kajang, Selangor, Malaysia.
Email: vigna@uniten.edu.my

Abstract

Frequency regulation of autonomous microgrids with intermittent renewables is a tedious task, which requires additional support from energy storage systems (ESS). Ideally, the system requires a faster-acting ESS to arrest the initial frequency deviation and high energy capacity ESS to restore the frequency to its nominal value. Pico hydel energy storage (PHES) is one such high energy capacity ESS developed from the agricultural pumping systems. However, PHES has a slower response and cannot switch rapidly between pumping and generation modes. Hence, this paper incorporates a battery with PHES to achieve a faster dynamic response and absorb high-frequency power dynamics. Additionally, a frequency regulation strategy with synchronverter control is proposed to mimic synchronous machines, especially to reduce the rate of change of frequency (ROCOF) and frequency nadir. Firstly, a small-signal modelling approach is proposed, and it was utilized to assess the system stability through eigenvalue analysis. Subsequently, transient simulations were carried out to gauge the performance of the synchronverter strategy with vector control for frequency regulation. As a result, the frequency nadir and ROCOF were substantially reduced with the synchronverter strategy compared to the vector control based on the simulation results.

1 | INTRODUCTION

Access to affordable and clean energy is one of the United Nations Sustainable Development Goals. Having said that, the remote communities in developing nations are deprived of stable electricity supply from the grid. The grid connectivity to such regions is hindered by topographical conditions (reserve forests, hilly hamlets), far proximity from the existing grid connection, low paying capacity, and dispersed settlements. Hence, autonomous microgrids comprising renewable energy sources (RES) along with local energy carriers act as a potential alternative to grid supply. However, the stochastic attribute of RES gives rise to concerns like poor load following, low inertia, volatile frequency, and voltage profiles. These issues are alleviated through backup or supporting reserves, often provided by energy storage systems (ESS). Pumped hydro storage (PHS) is a

tried and tested technology for bulk energy storage for over half a century. This argument is supported by its significant share of 168 GW, which accounts for approximately 97% of the total ESS installation worldwide. However, the construction of large PHS is limited by topographical conditions, longer planning, and commissioning period, along with socio-economic and ecological problems [1]. Therefore, it is perceived that small PHS development could be a better option over large PHS to exploit its high energy storage, longer lifetime, and low maintenance attributes.

Recently, abandoned mines, quarries, bore wells and dug wells have been retrofitted with suitable machinery to realize small PHS for applications in microgrid [2]. This paper explores one such configuration termed pico hydel energy storage (PHES) to provide energy storage with the existing agricultural pumping system. This configuration was developed with

an open well (lower reservoir), surface-level tank (upper reservoir), and reversible pump-turbine. Although PHES offers substantial energy storage, its slow response and inability to switch between modes (generation and pumping) deprive its ability to support the high-frequency power variations of intermittent RES. The high-frequency power variations could induce stress on the mechanical components and deteriorate their lifetime. Meanwhile, the size of the upper reservoir is constrained by water availability and the constructional cost of the upper reservoir. Thus, hybridizing it with a relatively faster battery energy storage system (BESS) would enable the configuration: (i) to have a better dynamic response, (ii) alleviate stress on mechanical components, and (iii) limit the size of the upper reservoir.

Among the issues related to the intermittent behaviour of RES, frequency regulation and virtual inertia are the main focus of this paper. Thus, the developed hybrid ESS (HESS) ensures enhanced frequency regulation, meanwhile emulating virtual inertia. Of late, HESS has received much attention from researchers for the frequency regulation of microgrids. A BESS and supercapacitor (SC) hybrid was adopted to regulate the frequency of a wind-powered microgrid [3]. In a hierarchical frequency regulation strategy that was proposed, SC handled the high-frequency power variations, while BESS handled low-frequency power variations. In another study, a similar HESS configuration was used for frequency regulation of an isolated power system with conventional generation and RES [4]. The control objectives were similar to the previous work, however, the load and source uncertainties were considered for dynamic studies. Recently, a combination of BESS and SC was employed in a grid-connected solar PV system to mitigate the power fluctuations and enhance the system stability [5]. A multivariable fuzzy logic control was proposed to optimize the time constant of the low pass filter for the coordinated operation of SC and BESS.

On the other hand, an HESS with BESS, SC, and flywheel energy storage (FES) was used to provide enhanced frequency reserve service to Great Britain's power system [6]. They used a fuzzy logic controller to control the HESS based on their state of charge (SoC). In another work, the superconducting magnetic energy storage (SMES) was hybridized with BESS to regulate the frequency of an autonomous microgrid [7]. The proposed dynamic droop control capitalized on the complementary characteristics of SMES and BESS for frequency regulation. Similarly, the BESS-SMES hybrid was used to smooth the power output of a wind farm using a moving average algorithm [8]. The algorithm split the power dynamics into low and high-frequency components to be allocated to BESS and SMES, respectively.

The aforementioned studies retained the BESS and shuffled the other ESS since their primary objective of hybridization was to extend the lifetime of BESS. However, the primary motive of this paper is to compound PHES with BESS to complement its slow response, inability to switch rapidly between modes, alleviate stress on mechanical components and limit the size of the upper reservoir. To achieve the hybridization objectives, BESS is expected to absorb the high-frequency power dynamics while leaving the lower frequency power dynamics to be handled by PHES.

Low inertia is another challenge in an autonomous microgrid whereby the static entities like solar PV, BESS, SC, and fuel cells do not have rotating inertia. Meanwhile, the variable speed wind turbines and PHS are categorized as quasi-static RES since they are decoupled from the grid by power converters. The maximum power extraction goal of RES forces the operating point to maximum power point, thus, hindering their frequency-dependent operation. Although, de-loading of RES has evolved in the past to facilitate their participation in frequency regulation [9, 10]. It can be argued that the continuous operation at a sub-optimal power point may lead to financial losses to the holding company.

Thanks to the virtual inertia emulation mechanism, which mimics the inertial response of the synchronous machine (SM). Introducing droop control was an initial step towards inducing frequency-dependent behaviour to the converters. Subsequently, numerous virtual inertia emulation techniques have been proposed [11], in which the most preferred techniques include (i) virtual synchronous machine (VISMA) [12], (ii) virtual synchronous generator (VSG) [13], and (iii) synchronverter [14]. VISMA and VSG techniques augment the swing equation to the vector control strategy, which projects them as current sources when viewed from the grid, unlike SM (voltage source) [15].

Eventually, the development of the synchronverter combining an ESS and control algorithm exhibited all the desired properties of SM and remained the closest resemblance to SM. It has the vital characteristics of SM like rotational inertia, oscillation damping and self-synchronization and these properties maintain the stability of large power systems. Furthermore, the synchronverter does not suffer from instability due to the frequency derivative term, requires PLL only for initial synchronization and acts as a voltage source. Henceforth, the synchronverter has been employed for several applications including wind electric system [16], solar PV [17], HVDC systems [18], electric vehicle charger [19], BESS [20], and STATCOM [21].

While discussing the virtual inertia control strategies, it is worthwhile to review its recent application in the control and coordination of HESS. Recently, a single-phase synchronverter was employed in a rooftop solar PV system to provide ancillary service to the grid [22]. The developed virtual inertia strategy controlled a HESS consisting of BESS and SC, which catered for medium and high-frequency power dynamics, respectively. Utilizing the same HESS combination, a damping and virtual inertia emulation technique was proposed for frequency and dc link voltage regulations of hybrid ac/dc microgrid. The proposed strategy utilized the droop coefficients of parallel operating inverters to emulate damping and virtual inertia at the dc link [23]. Another research on hybrid ac/dc microgrid implement distributed ESS for dc link voltage and frequency controls. The current references to the current controller of the interlinking converter were derived from the swing equation of machines [24].

The review of literature presented reveals that there are limited works dealing with virtual inertia control for HESS in

general and it is yet to be researched widely. Specifically, the PHES-BESS hybrid is yet to be investigated for frequency regulation to the best of the authors knowledge. Hence, this paper aims to examine the performance of the PHES-BESS hybrid with the existing vector control and enhance the performance with synchronverter control in an autonomous microgrid. In line with the discussions made, the main contributions of this paper include:

1. A novel frequency regulation strategy utilizing the PHES-BESS hybrid with synchronverter control is proposed.
2. The small-signal modelling approach is proposed for HESS, and the stability is analysed through eigenvalue analysis.
3. The inherent behaviour of PHES in decoupling its power-sharing dynamics with BESS is elucidated through the frequency response and spectral decomposition techniques.

The paper is organized as follows: Section 2 describes the system configuration and modelling, followed by Section 3, which presents the proposed frequency regulation strategy. Subsequently, Section 5 analyses the transient performance with the synchronverter strategy, and Section 6 concludes the paper.

2 | MODELLING OF SYSTEM COMPONENTS

2.1 | Microgrid with hybrid energy storage system

The microgrid comprises solar PV, PHES, BESS, and residential load (Figure 1). The base load was catered by a solar PV plant of 44 kWp capacity, which produces 36 kWac at nominal irradiation of 900 Wm^{-2}. A dc-dc converter with a maximum power extraction control and a voltage source converter (VSC) configuration were adopted to control the solar PV. Meanwhile, a 5 kW and 18 kWh PHES along with a 5 kW and 5 kWh BESS were employed to form the HESS, which supports the microgrid with the proposed control algorithm.

BESS was connected to the microgrid using synchronverter control to act as a grid forming unit. On the contrary, the PHES was operated at variable speed using a machine control converter (MCC), and it was integrated into the microgrid with a grid coupling converter (GCC). The MCC optimizes the rotor speed for maximum power extraction during generation operation, whereas it precisely controls the power absorbed from the microgrid in the pumping mode. Notably, the GCC of PHES operates as a grid supporting converter by following the frequency and voltage references of the BESS-synchronverter in both modes of operation. The microgrid controller lies over the local control strategies and overlooks the operation and coordination of microgrid components. It observes the reservoir level of PHES and SoC of BESS to ensure that they remain within limits at all times. Since this paper is focused on local control of PHES and BESS, the SoC and reservoir levels are assumed to be within acceptable limits.
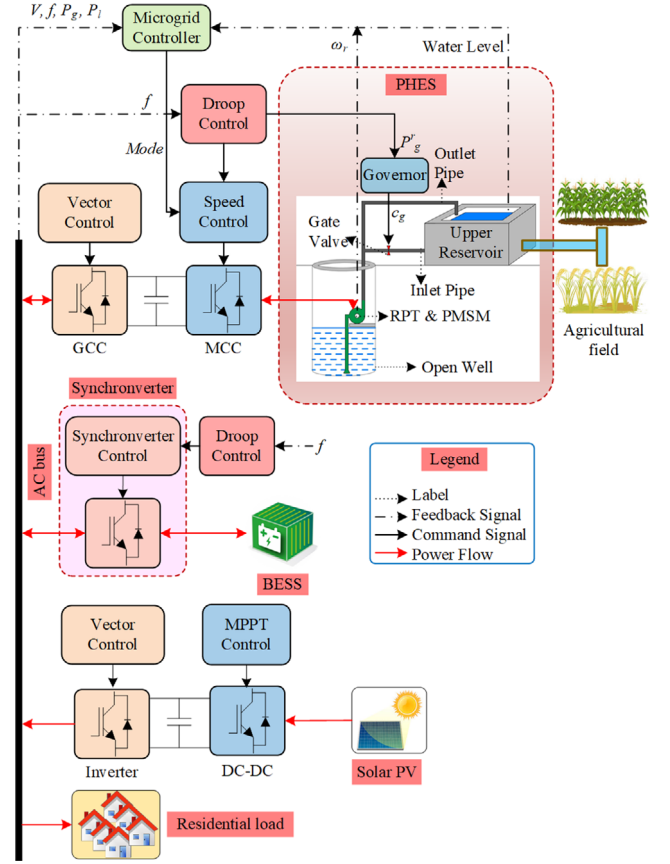
FIGURE 1 Microgrid with solar PV and PHES-BESS hybrid

2.2 | Pico hydel energy storage

2.2.1 | Hydraulic turbine

The normalized discharge (q_t) equation neglecting the frictional loss was expressed by Equation (1), where, A_p, l_p, h_t, Q_{nom} and H_{nom}, are the cross-section of the penstock (m^2), length of the penstock (m), normalized head (m), the nominal values of discharge (m^{3}s^{-1}) and head (m), respectively, $\tau_{ws} = \frac{l_p Q_{nom}}{A_p g H_{nom}}$ [25].

$$\frac{dq_t}{dt} = \frac{1}{\tau_{ws}}(1 - h_t) \tag{1}$$

The servo mechanism determines the water discharge rate that is proportional to the gate position (c_g) Equation (2).

$$q_t = c_g \sqrt{h_t} \tag{2}$$

The mechanical output power of the turbine with the gate valve having damping coefficient, D_t, was expressed by Equation (3), where, η_t is the turbine efficiency, and ω_t is speed (rad/s).

$$P_t = A_t \cdot q_t \cdot h_t - D_t c_g \Delta \omega_t; \; A_t = \eta_t \cdot \rho_w \cdot g \tag{3}$$

Linearizing Equations (1), (2), (3) and solving for Δq_t, Δh_t will yield Equation (4).

$$\Delta q_t = -\frac{\Delta h_t}{s\tau_{ws}}\,\Delta h_t; \quad = -\frac{\frac{\partial q_t}{\partial c_g}\Delta c_g}{\frac{1}{s\tau_{ws}} + \frac{\partial q_t}{\partial h_t}} \qquad (4)$$

Eventually, substituting Equation (4) into the linearized Equation (3) will yield the linearized turbine Equation (5), whereby the partial derivatives in Equation (5) were computed around an operating point, where $\frac{\partial q_t}{\partial h_t} = \frac{1}{2}\frac{c_{g0}}{\sqrt{h_{t0}}}$, $\frac{\partial q_t}{\partial c_g} = \sqrt{h_{t0}}$, $\frac{\partial P_t}{\partial q_t} = A_t h_{t0}$, $\frac{\partial P_t}{\partial h_t} = A_t q_{t0}$, $\tau'_{ws} = \tau_{ws}\frac{q_{t0}}{h_{t0}}$, (subscript '0' represents the initial point).

$$\frac{\Delta P_t}{\Delta c_g} = \frac{\left(\frac{\partial q_t}{\partial c_g}\frac{\partial P_t}{\partial q_t}\right) - \left(s\tau_{ws}\frac{\partial P_t}{\partial h_t}\frac{\partial q_t}{\partial c_g}\right)}{1 + s\tau_{ws}\frac{\partial q_t}{\partial h_t}} = A_t h_{t0}^{\frac{3}{2}}\left(\frac{1 - s\tau'_{ws}}{1 + \frac{s\tau'_{ws}}{2}}\right) \qquad (5)$$

2.2.2 | Hydraulic governor

The governor controls the water discharge rate with a servo mechanism to generate the required power. It was augmented with a droop control (R_{dp}) to respond to grid frequency (ω_g) variations and adjust the power set point (ΔP_g^r) Equation (6).

$$\Delta P_g^r = \frac{1}{R_{dp}}\Delta\omega_g \qquad (6)$$

The PI controller sets the discharge reference (Δq_t^r) by acting on the power error (ΔP_{gp}) Equation (7), subsequently, the servo mechanism varies the gate valve position with a time delay (τ_g) Equation (8).

$$\Delta q_t^r = \left(K_{pg} + \frac{K_{ig}}{s}\right)\Delta P_{gp} \qquad (7)$$

$$\Delta c_g = \frac{1}{\sqrt{h_{t0}}}\left(\frac{1}{1 + s\tau_g}\right)\Delta q_t^r \qquad (8)$$

2.3 | Battery energy storage system

The generic model of battery used in this paper represents an ideal controllable dc voltage source with internal resistance [26]. The no-load voltage (v_b) was expressed as a non-linear function of the SoC of BESS Equation (9), where, v_{b0} is the emf of battery (V); κ is the polarisation voltage (V); ζ is the exponential zone voltage (V); ξ is the reciprocal of time constant (A/h); σ is the total battery capacity (Ah).

$$v_b = v_{b0} - \kappa\frac{1}{SoC} + \zeta^{-\xi\sigma(1-SoC)} \qquad (9)$$
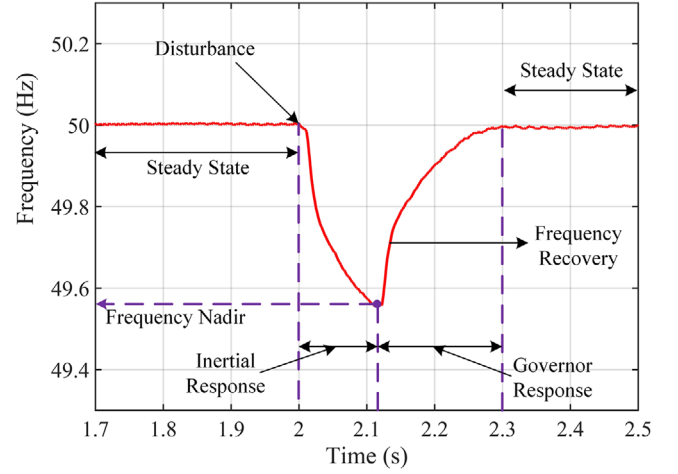
FIGURE 2   Time discretization of primary frequency response

The instantaneous SoC computation involves the deduction of the net charge exchanged by the battery from its total capacity Equation (10). In short, it is the net charge available in the BESS at any instant, and the time-integral component in Equation (10) indicates the state of discharge (SoD).

$$SoC\,(t) = \sigma - \int_0^t i_b dt \qquad (10)$$

3 | PROPOSED FREQUENCY REGULATION STRATEGY

3.1 | Frequency regulation in microgrid

The instantaneous power balance of the system dictates its frequency as per the swing equation of electromechanical systems Equation (11), where f_n, P_g, P_l, and H_{eq} are the nominal frequency (Hz), power generated (W), power consumed (W), and equivalent inertia of the system (s), respectively.

$$\frac{df}{dt} = \frac{f_n}{2H_{eq}}\left(P_g - P_l\right) \qquad (11)$$

The resistance offered by SM to change its speed for a rapid change in power is quantified as the inertia of the power system. The SM absorbs the instantaneous power change through storing or releasing the kinetic energy in its rotor inertia, thus, curtailing the sudden change in system frequency. Eventually, it is possible to time discretize the primary frequency response of the power system with decoupled inertial and governor responses (Figure 2). During a contingency event, the inertia of the rotating machines arrests the initial frequency excursion, followed by the governor response.

The conventional power system's inertia with SMs is considerably high as opposed to the current system with an increased share of static RES. This effect is more pronounced

in the autonomous microgrid powered by RES than the inter-connected power system, owing to the absence of rotating machines. Although the droop-controlled power converters mimic the behaviour of mechanical governors, they fail to exert the inertial response. Thus, the low inertia of microgrid results in steep ROCOF and increased frequency nadir/peak leading to poor frequency regulation.

3.2 | Virtual inertia

The degradation in system inertia due to static RES or quasi-static RES entails virtual inertia emulation in a microgrid. The proposed frequency regulation strategy aims to increase the equivalent inertia of the microgrid by operating BESS with synchronverter control. Simultaneously, utilizing PHES with vector control for injecting the significant share of power required for a longer duration. Thus, the dynamic frequency variation of the microgrid is affected by the proposed HESS as per Equation (12), where P_{pv} and P_l represent solar PV power and load, respectively. Meanwhile, the power exchanged by BESS (P_{eb}) and PHES (P_{ep}) is the function of their droop coefficients R_{db} and R_{dp}, respectively.

$$\frac{df}{dt} = \frac{f_n}{2\left(H_{eq} + H_v\right)}\left(P_{pv} - P_l \pm R_{db}P_{eb} \pm R_{dp}P_{ep}\right) \quad (12)$$

Eventually, the virtual inertia contributed by the BESS-synchronverter increases the equivalent inertia of the microgrid (H_{eq}), by an amount H_v, which is the virtual inertia constant.

According to G59 guidelines by Energy Networks Association, UK, the setting for ROCOF (R_c) for microgrids should be a minimum of 0.5 Hz/s and the frequency should be within 50 ± 1.5 Hz [27, 28]. Hence, R_c is set to 0.5 Hz/s for computing the necessary virtual inertia of the microgrid [28]. Meanwhile, the values of nominal power (P_n) and nominal frequency (ω_n) were 54 kW and 314.15 rad/s, respectively. Considering a load change (ΔP) of 5 kW and substituting the values in Equation (13) yielded the value of the required virtual inertia constant as 4.62 s. Consequently, using Equation (14), the value of virtual inertia (J_v) was derived as 5 kgm^2.

$$H_v = \frac{\Delta P f_n}{2 P_n R_c} \quad (13)$$

$$J_v = \frac{H_v P_n}{0.5 \omega_n^2} \quad (14)$$

However, H_v is limited by the frequency recovery period, which can be tuned to meet system requirements. For instance, a large H_v may reduce the frequency nadir and ROCOF while deteriorating the frequency recovery dynamics. Meanwhile, a small H_v may provide fast frequency recovery, thereby compromising on the ROCOF, hence, a trade-off should be met to satisfy both scenarios. In this paper, the trade-off was manually

FIGURE 3 Synchronverter control strategy for BESS

achieved by observing the system step response. Nevertheless, online optimization can be utilized for that purpose by considering the ROCOF and frequency deviation in real-time and it is left for further research.

3.3 | Synchronverter control of BESS

Synchronverter comprises an ESS, a VSC, and a control algorithm, whose dynamic model is based on the round rotor SM with distributed winding. The detailed empirical model of the system can be found in [14], while this paper only explains the control strategy. The synchronverter has two independent loops for real and reactive power control, as illustrated in Figure 3. However, only the real power regulation loop was considered for small-signal modelling as frequency regulation is the main interest of this paper. The real power regulation was achieved through the swing equation of rotating machines Equation (15); where, ω, P_{mb}, P_{eb}, and D_p, represent grid frequency (rad/s), mechanical power (W), electrical power (W), and damping coefficient, respectively.

$$\frac{d\omega}{dt} = \frac{1}{J_v\omega}\left(P_{mb} - P_{eb} - D_p\left(\omega_n - \omega\right)\right) \quad (15)$$

Equation (16) was yielded by linearizing Equation (15).

$$\Delta P_{mb} - \Delta P_{eb} = J_v\omega\frac{d\Delta\omega}{dt} + D_p\Delta\omega \quad (16)$$

The synchronverter was augmented with a droop controller to translate the change in system frequency to the required power change. Hence, Equation (17) represented the linearized droop equation derived from the actual droop equation.

$$\omega = \omega_n - R_{db}P_{mb} \Rightarrow \Delta P_{mb} = \frac{\Delta\omega}{-R_{db}} \quad (17)$$

Substituting Equation (17) in (16) and applying Laplace transform will yield Equation (18), from which the transfer function

of the real power loop (RPL) was derived Equations (19), (20), where P_{eb} was computed from the line voltage (v_g) and line current (i_{gb}). Subsequently, the output frequency of the synchronverter was integrated to obtain the angle (θ_s) for synchronization of other units in the microgrid. Although the reactive power loop (RePL) is not of interest here, it was used to generate the reference voltage magnitude (e_s) for the microgrid. Hence, the virtual flux (ϕ_v) was generated using net reactive power injection ($Q_{gb}^r - Q_{gb}$) and voltage deviation ($v_g^r - v_g$) by integrating with a constant (k_q).

$$-\Delta P_{eb} = J_v \omega s \Delta \omega + D_p \Delta \omega + \frac{\Delta \omega}{R_{db}} \qquad (18)$$

$$\Rightarrow \frac{\Delta P_{eb}}{\Delta \omega} = -\left(J_v \omega s + \left(D_p + \frac{1}{R_{db}}\right)\right) \qquad (19)$$

$$\therefore G_{syn}(s) = \frac{\Delta \omega}{\Delta P_{eb}} = -\left(\frac{1}{1 + s\frac{J_v \omega}{D'_p}}\right); \quad D'_p = \left(D_p + \frac{1}{R_{db}}\right) \qquad (20)$$

3.4 | Vector control of PHES

The active power control of PHES involves two distinct entities, a hydraulic governor and a two-stage VSC. The hydraulic governor and MCC control the active power output, while the GCC facilitates grid integration. Meanwhile, PHES supports the microgrid based on the voltage and frequency references set by the BESS-synchronverter, whereby the power required to maintain the frequency is exchanged.

$$\omega = \omega_n - R_{dp} P_{mp} \Rightarrow \Delta \omega = -R_{dp} \Delta P_{mp} \qquad (21)$$

Similar to the synchronverter control, the droop control was integrated with the hydraulic governor to set the power reference for PHES. Hence, Equation (21) represented the linearized droop equation, which was obtained from the actual droop equation. Unlike the instantaneous droop response of BESS, the droop response of PHES suffers a mechanical time delay of the governor. Hence, the droop coefficient was expressed as a function of governor response with the time constant (τ_g) (22). However, the time delay of the PI controller is negligible relative to the mechanical time constant of the servo mechanism (τ_g).

$$R_{dp}(s) = |R_{dp}|\left(\frac{1}{1 + s\tau_g}\right) \qquad (22)$$

On the other hand, the GCC employed voltage oriented control with nested voltage and current controllers to modulate the dc-link voltage and enable maximum power exchange with the
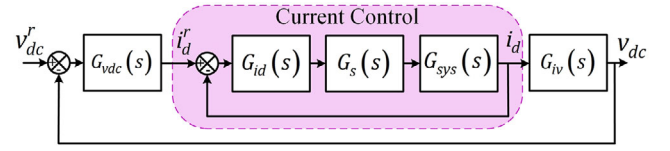

FIGURE 4 *d* axis control loop of voltage oriented control for PHES

microgrid (Figure 4). Since the *d* axis current and voltage determine the net active power flow (23), the dynamics of the *q* axis control loop is neglected here.

$$P_{ep} = \frac{3}{2} v_{dp} i_{dp} \qquad (23)$$

The inner current controller with proportional gain (k_{pi}) and integral gain (k_{ii}) regulates the current corresponding to the reference value set by the voltage controller. The dynamics of the current controller is affected by the dynamics of the LC filter ($G_{sys}(s)$) having inductance (L_{fp}) and resistance (R_{fp}), along with the PI controller ($G_{id}(s)$) Equation (24). Meanwhile, the grid inductance also adds to the filter inductance and contributes to the dynamics of the controller. Furthermore, the delay introduced due to sampling ($G_s(s)$) was approximated as a first-order lag with a time constant τ_s Equation (24).

$$\frac{\Delta i_d}{\Delta i_d^r} = \frac{G_{id}(s) G_s(s) G_{sys}(s)}{1 + G_{id}(s) G_s(s) G_{sys}(s)} \qquad (24)$$

Finally, the closed-loop transfer function of the inner current controller Equations (25), (26) was reduced to Equation (27), where, $A = L_{fp}\tau_s$, $B = R_{fp}\tau_s + L_{fp} + k_{pi}$, $C = k_{ii} + R_{fp}$.

$$\frac{\Delta i_d}{\Delta i_d^r} = \frac{\left(k_{pi} + \frac{k_{ii}}{s}\right)\left(\frac{1}{R_{fp}+sL_{fp}}\right)\left(\frac{1}{1+s\tau_s}\right)}{1 + \left(k_{pi} + \frac{k_{ii}}{s}\right)\left(\frac{1}{R_{fp}+sL_{fp}}\right)\left(\frac{1}{1+s\tau_s}\right)} \qquad (25)$$

$$G_{id}(s) = \frac{\Delta i_d}{\Delta i_d^r} = \frac{(sk_{pi} + k_{ii})}{s^2 L_{fp}\tau_s + s\left(R_{fp}\tau_s + L_{fp} + k_{pi}\right) + \left(k_{ii} + R_{fp}\right)} \qquad (26)$$

$$G_{id}(s) = \frac{(sk_{pi} + k_{ii})}{As^2 + Bs + C} \qquad (27)$$

The outer voltage control loop intends to control the dc-link voltage at a level greater than 1.6 times the line voltage. The dc-link voltage was regulated through the voltage controller having proportional gain (k_{pv}) and integral gain (k_{iv}), by maintaining the power balance across the dc-link capacitor. The active power exchanged to the grid is proportional to the *d* axis voltage (v_{dp}), and current (i_{dp}), thus, i_{dp} was manipulated to control the dc-link voltage. The dynamics of the voltage control loop include

its PI controller ($G_{vdc}(s)$), the inner loop ($G_{id}(s)$), and the dc-link ($G_{iv}(s)$) Equation (28).

$$\frac{\Delta v_{dc}}{\Delta v_{dc}^r} = \frac{G_{vdc}(s)\, G_{id}(s)\, G_{iv}(s)}{1 + G_{vdc}(s)\, G_{id}(s)\, G_{iv}(s)} \qquad (28)$$

The time constant of the outer loop was set higher than the current control loop, allowing it to settle after the inner control loop for stable operation. Finally, the transfer function of the voltage controller Equations (29), (30) was reduced to Equation (31), where, $\alpha = AC_{dp}$, $\beta = BC_{dp}$, $\gamma = CC_{dp} + k_{pv}k_{pi}$, $\vartheta = k_{ii}k_{pv} + k_{iv}k_{pi}$, $\psi = k_{iv}k_{ii}$.

$$\frac{\Delta v_{dc}}{\Delta v_{dc}^r} = \frac{\left(k_{pv} + \frac{k_{iv}}{s}\right)\left(\frac{sk_{pi}+k_{ii}}{As^2+Bs+C}\right)\left(\frac{1}{sC_{dp}}\right)}{1 + \left(k_{pv} + \frac{k_{iv}}{s}\right)\left(\frac{sk_{pi}+k_{ii}}{As^2+Bs+C}\right)\left(\frac{1}{sC_{dp}}\right)} \qquad (29)$$

$$G_{gcc}(s) = \frac{\Delta v_{dc}}{\Delta v_{dc}^r} = \frac{s^2 k_{pv}k_{pi} + s\left(k_{ii}k_{pv} + k_{iv}k_{pi}\right) + k_{iv}k_{ii}}{\alpha s^4 + \beta s^3 + \gamma s^2 + \vartheta s + \psi} \qquad (30)$$

Since the PHES was operated at variable speed, the dynamics of GCC was included in Equation (21) to derive its frequency response Equation (31).

$$\frac{\Delta \omega}{\Delta P_{mp}} = -\left|R_{dp}\right|\left(\frac{1}{1 + s\tau_g}\right)\left(\frac{s^2 k_{pv}k_{pi} + s\left(k_{ii}k_{pv} + k_{iv}k_{pi}\right) + k_{iv}k_{ii}}{\alpha s^4 + \beta s^3 + \gamma s^2 + \vartheta s + \psi}\right) \qquad (31)$$

4 | STEP RESPONSE AND STABILITY ANALYSES

The dynamic performance and small-signal stability of the system can be well appreciated with the step response and eigenvalue analysis, respectively. So, the step responses and eigenvalue loci of the system were obtained by varying the parameters, J_v and τ_g, which affect the system dynamics. Meanwhile, these analyses were also used to fine-tune the parameters obtained through empirical relationships. The range of variation was determined by considering the lower and upper bound values that would accommodate the theoretically calculated value of J_v and τ_g.

4.1 | J_v variation ($\tau_g = 0.2$ s)

The step response obtained by varying J_v revealed that a large value of J_v resulted in no peak overshoot, increased settling time, and system oscillations were damped up to, $J_v = 0.5$ kgm^2 (Figure 5). However, the system indicated peak overshoot for $J_v < 0.5$ kgm^2, which corresponded to an under-damped scenario, whereby supporting the argument on H_v in Section 3.2. Meanwhile, the corresponding eigenvalue loci indicated that the
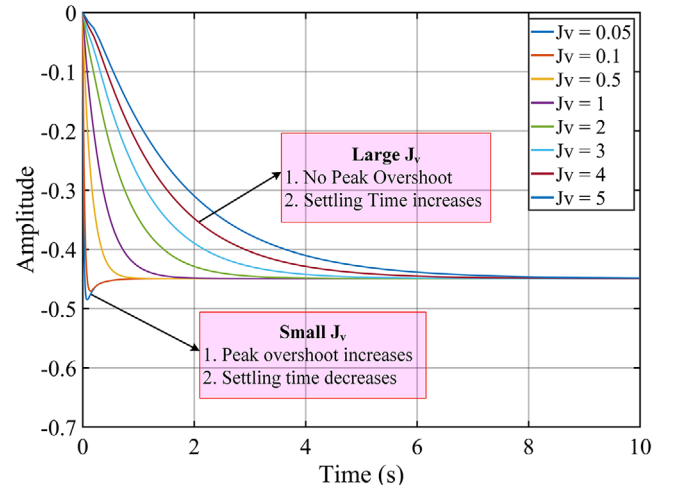

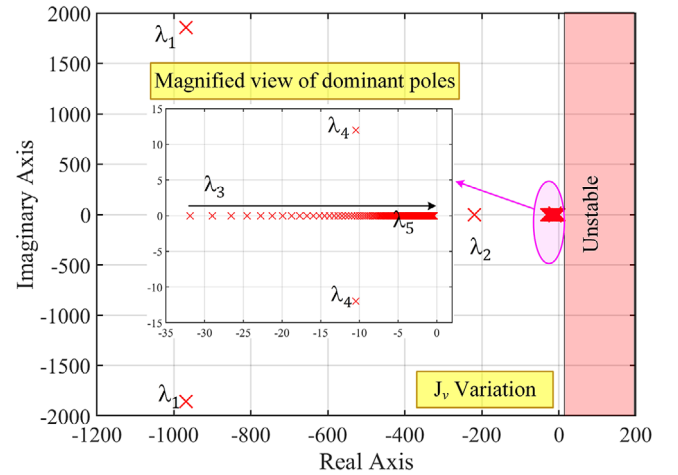**FIGURE 5** System step response for J_v variation

FIGURE 6 Eigenvalue loci of the system for J_v variation

system remained stable when J_v varied from 0.05 to 10 kgm^2 (Figure 6).

4.2 | τ_g variation ($J_v = 5$ kgm^2)

The effects of τ_g variation indicated similar responses to the previous case. For instance, a large τ_g behaves as a virtual inertia component by delaying the power change, whereas a small τ_g increases the peak overshoot. An interesting phenomenon was observed in the settling time for a small τ_g, which contradicted the behaviour observed in the previous case (Figure 7). A small τ_g demonstrated a poor damping effect due to the frequent movement of the gate, whereby the settling time was increased, Equation (8). The eigenvalue loci of the system vouched for the system stability even when τ_g varied over a wide range from 0.05 to 0.5 s (Figure 8).
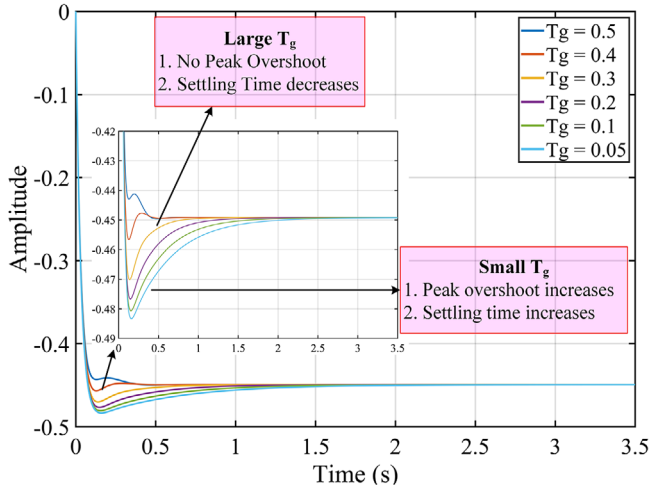
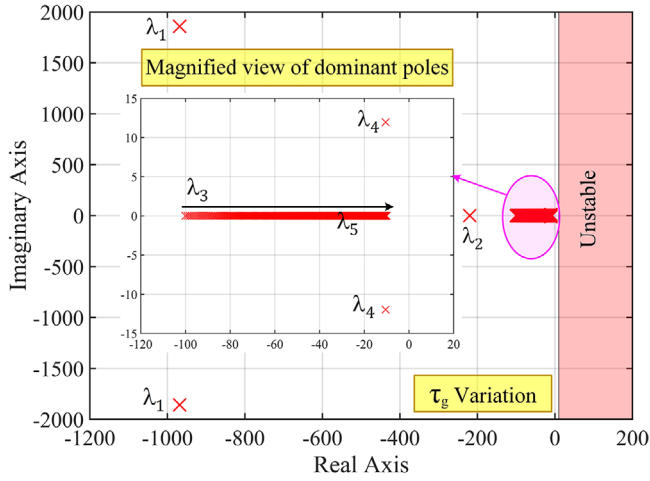**FIGURE 7** System step response for τ_g variation

FIGURE 8 Eigenvalue loci of the system for τ_g variation

TABLE 1 Parameters of PHES

Parameters	Value
PHES power	5 kW
Upper reservoir volume	450 m^3
Energy storage capacity	18 kWh
Rated head	16–20 m
Rated discharge	25–30 L/s
dc link voltage	600 V
Line voltage	400 V
τ_g	0.05 s
$k_{pv}, k_{iv}, k_{pi}, k_{ii}$	5.23, 142.5, 4.6, 103.21

TABLE 2 Parameters of BESS

Parameters	Value
BESS power	5 kW
BESS energy	5 kWh
dc link capacitor	25 mF
dc link voltage	600 V
Line voltage	400 V
H_v	4.62 s
J_v	5 kgm^2
D_p	300
Switching frequency	5 kHz
LCL filter	11 mH, 0.62 μF, 6.6 mH
Line reactance,resistance	0.0238 Ohm/km,0.342 Ohm/km

5 | PERFORMANCE ANALYSIS

The performance of the system was assessed through transients simulated using MATLAB/Simulink software by considering both the generation and pumping scenarios of PHES. Firstly, the dynamic performance of the system was evaluated using frequency metrics like ROCOF and frequency nadir through fault analysis, load and irradiation changes. It is worth mentioning that the ROCOF value was computed using the first-order difference algorithm and it was passed through a filter to eliminate the noise [29]. The expected values of ROCOF and frequency nadir/peak should lie within 0.5 Hz/s and 50 ± 1.5 Hz, respectively and these values were used for validating the proposed control strategy.

Subsequently, the power decoupling between PHES and BESS was analysed through the Fast Fourier Transform (FFT) analysis and frequency response analysis of the system. The parameters of PHES and BESS used for time-domain simulations are furnished in Tables 1 and 2, respectively.

5.1 | PHES in generation

5.1.1 | Fault analysis

When operated in generation mode, PHES contributed to a major portion of the deficit power. Meanwhile, BESS mitigated the faster varying power components, which cannot be handled by PHES. A real-time irradiation pattern with random variation, having a mean value of 800 W/m^2 was fed to the solar PV system (Figure 9a), which generated 32 to 33 kW (Figure 9f). Meanwhile, the load on the system was maintained at 35.5 kW (Figure 9g). Subsequently, a significant share of 3.2 kW was contributed by PHES (Figure 9e), whereas BESS injected 300 W (a faster varying power share) (Figure 9d). The power exchanged by BESS oscillated between positive and negative values to maintain the frequency of the microgrid.

The system performance was analysed by applying a 100 ms three-phase fault at $t = 2$ s. The results indicated that the synchronverter control measured a minimum ROCOF of approximately ±0.25 Hz/s compared to the ±2.5 Hz/s with the vector control (Figure 9c). Meanwhile, the synchronverter control restricted the frequency nadir to 49.97 Hz versus 49.5 Hz with the vector control (Figure 9b). Consequently, the
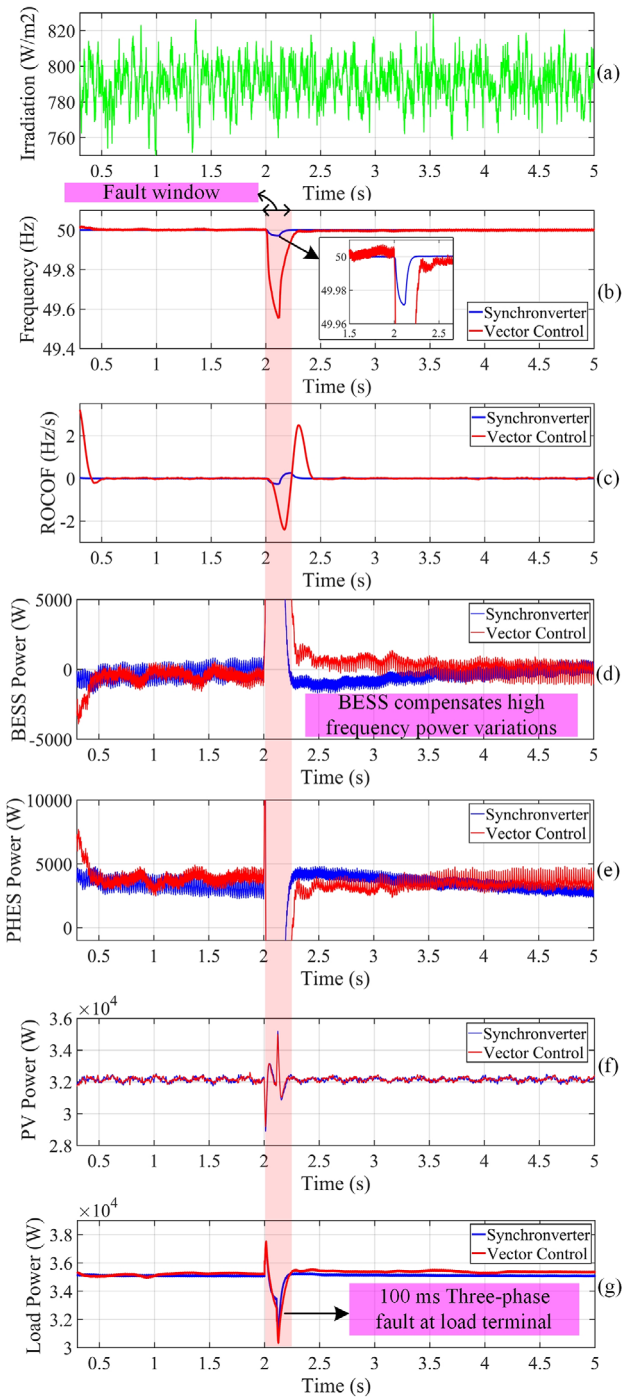
FIGURE 9 Fault analysis while PHES is in generation mode: (a) solar irradiation, (b) frequency, (c) ROCOF, (d) BESS power, (e) PHES power, (f) PV power, and (g) load power

synchronverter control restored the frequency faster at 2.22 s, compared to the vector control, which took 170 ms longer to restore the frequency at 2.39 s (Figure 9b).

It can be concluded that the vector control showed an immediate drop in frequency with higher ROCOF and frequency nadir, which is primarily due to the absence of an inertial component in the vector control strategy. The response time of the vector control depends on the delay due to power electronic

converters and the time constants of voltage and current control loops. However, the dynamic response of the synchronverter is governed by the virtual inertia in the control loop, which does not allow sudden change power and hence the system frequency. This explanation holds good for all the cases explained henceforth.

5.1.2 | Load and irradiation changes

In this scenario, the transient performance of the system was assessed by varying the load and irradiance after the steady-state was attained. At a steady-state, the irradiance was maintained at an average value of 800 W/m^2 (Figure 10a) that generated 32.5 kW from solar PV (Figure 10f). Meanwhile, the load was maintained at 35 kW (Figure 10g) and the deficit of 2.5 kW was injected by PHES (Figure 10e), while BESS only supports the high-frequency power variations (Figure 10d). The first transition was induced by increasing the load from 35 to 40 kW at $t = 2$ s, resulting in a deficit of 7.5 kW. The BESS immediately responded to the transition by injecting 2.5 kW, whereas the major portion of 5 kW was served by PHES.

The consequence of the first transition was an under frequency event due to the deficit in power. The vector control resulted in a frequency drop from 50.02 to 49.998 Hz, whereas the synchronverter control does not show a considerable change in frequency (Figure 10b). Similarly, ROCOF was 0.022 Hz/s with synchronverter control as opposed to 0.15 Hz/s with VC (Figure 10c).

The second transition was induced by changing the irradiation from 800 to 650 W/m^2 (Figure 10a), resulting in PV power reduction from 32.5 to 26 kW at $t = 4$ s (Figure 10f). The load was switched back to 35 from 40 kW to simulate the effect of change in irradiation (Figure 10g). A deficit of 9 kW was left to be met by PHES and BESS from their reserve capacity. The PHES takes up the major share of 5 kW (Figure 10e) and the remaining 4 kW was satisfied by BESS (Figure 10d). Notably, the effect of varying irradiation on frequency was only evident with vector control resulting in a nadir of 49.94 Hz, while the synchronverter control did not show an apparent change (Figure 10b).
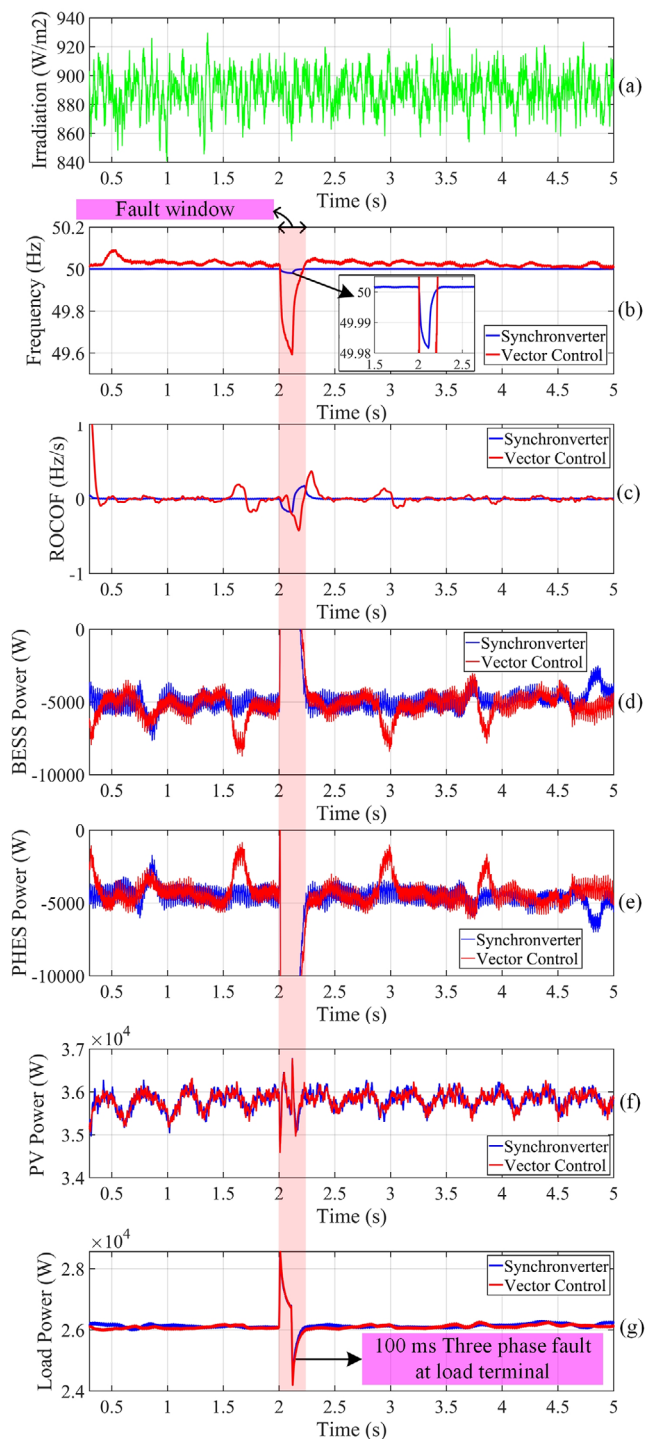
5.2 | PHES in pumping

5.2.1 | Fault analysis

PHES was also operated in pumping mode to absorb the excess power generated from solar PV, while BESS was controlled to absorb high-frequency power dynamics. The irradiance was varied between 920–860 W/m^2 (Figure 11a) to emulate the real-time scenario, and the corresponding solar PV output was between 35 to 36 kW (Figure 11f). The load was maintained at 26 kW, allowing the excess 9 to 10 kW to be absorbed by HESS (Figure 11g). The PHES absorbed 5 kW (Figure 11e), while BESS absorbed the remaining power, which varied between 4 to 5 kW (Figure 11d).
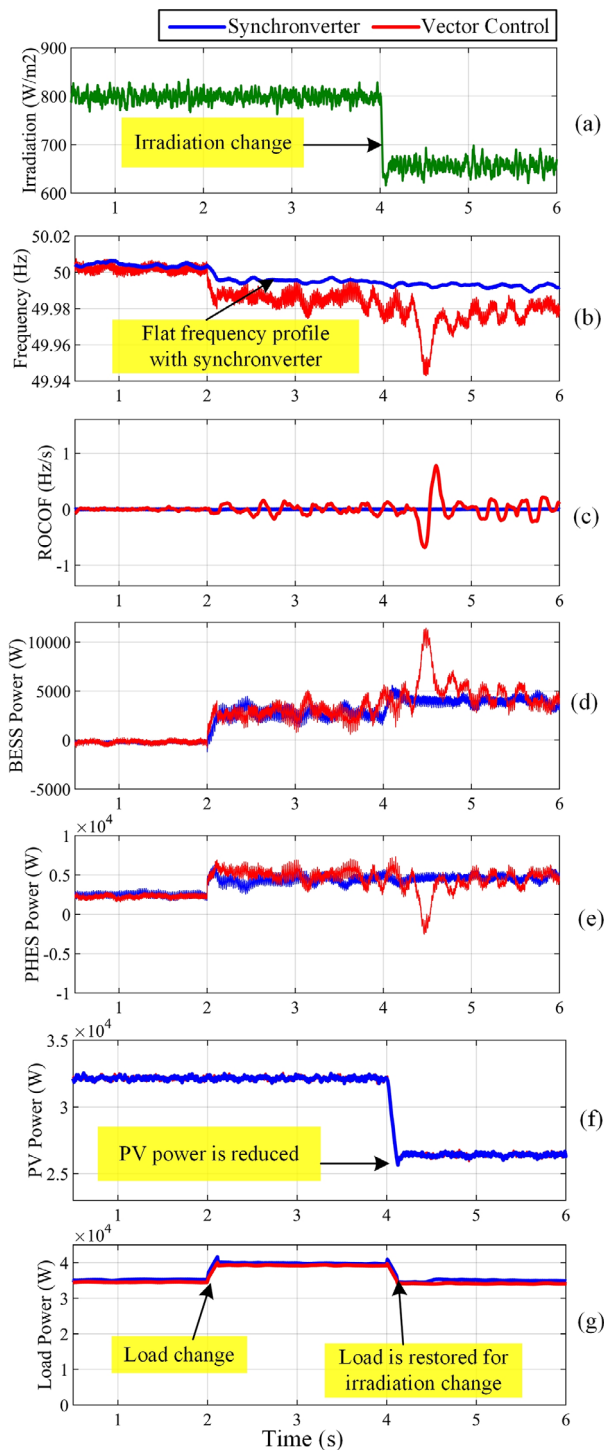
FIGURE 10 Performance analysis under load and irradiation changes while PHES is in generation mode: (a) solar irradiation, (b) frequency, (c) ROCOF, (d) BESS power, (e) PHES power, (f) PV power, and (g) load power

FIGURE 11 Fault analysis while PHES is in pumping mode: (a) solar irradiation, (b) frequency, (c) ROCOF, (d) BESS power, (e) PHES power, (f) PV power, and (g) load power

Similar to the previous case, at $t = 2$ s, a 100 ms three-phase fault was simulated at the load terminals. Consequently, the frequency was constrained to 49.98 Hz with the synchronverter control, while the frequency plummeted to 49.61 Hz with the vector control (Figure 11b). Meanwhile, a higher ROCOF of ± 0.4 Hz/s was observed with the vector control versus ± 0.17 Hz/s for the synchronverter control (Figure 11c). Subsequently, the frequency restoration also followed a similar pattern, as seen in the previous case. The synchronverter control restored the frequency faster at 2.219 s, while the vector control took 243 ms more to restore the frequency at 2.462 s (Figure 11b).

5.2.2 | Load and irradiation changes

In this case, the transient performance of the system was analysed by varying the load and irradiance at a steady state. Initially, the irradiance was maintained at an average value of 920 W/m² (Figure 12a) that generated 37.5 kW from solar PV (Figure 12f). Meanwhile, the load was maintained at 37.5 kW (Figure 12g), leaving an excess of 10 kW. The excess power was absorbed by PHES and BESS equally, consuming 5 kW each (Figure 12e and Figure 12d). The first transition was induced by increasing the load from 27.5 to 30 kW at $t = 2$ s, resulting in a deficit of 7.5 kW (Figure 12f). Consequently, BESS immediately responds to the transition by reducing its power consumption from 5 to 2.5 kW (Figure 12d). At the same time, PHES continued to consume 5 kW without changing its operating point (Figure 12e). The consequence of the first transition was an under frequency event due to the deficit in power. The vector control resulted in a frequency drop from 50.03 to 49.998 Hz, whereas synchronverter control did not show considerable frequency changes (Figure 12b). Meanwhile, ROCOF was 0.05 Hz/s with synchronverter control and 0.2 Hz/s with vector control (Figure 12c).

The second transition was induced by changing the irradiation from 920 to 720 W/m² (Figure 12a), resulting in PV power reduction from 37.5 to 30.5 kW at $t = 4$ s (Figure 12f). The load was switched back to 27.5 from 30 kW to simulate the effect of change in irradiation (Figure 12g). A deficit of 2.5 kW was left to be consumed by PHES and BESS for their charging. The PHES consumed a significant share of 2.5 kW (Figure 12e) and BESS consumed the remaining 0.5 kW (Figure 12d). Notably, the effect of varying irradiation on frequency was only observed with vector control resulting in a nadir of 49.97, while synchronverter control did not exhibit significant change (Figure 12b).

5.3 | Decoupling of power-sharing dynamics

According to Equation (3), the water discharge rate can effectively control the power output of PHES through governor action. So, the principle of power decoupling was based on the inherent mechanical time delay of the hydraulic governor, which resembles a low pass filter. According to Equation (22), the droop control of PHES suffers the first-order delay due to the servo mechanism that smoothens the water discharge rate into the turbine. Hence, PHES only catered to the low-frequency power dynamics, while BESS absorbed the high-frequency power dynamics with its fast droop response. The closed-loop frequency responses of PHES and BESS substantiated the facts mentioned above (Figure 13). Firstly, the droop function of PHES had the characteristics of a low pass filter with a cut-off frequency of 120 rad/s (19.09 Hz), thus, contributing to the inherently low-frequency response. Secondly, although BESS allowed low-frequency components below 19.09 Hz, its gain (63 dB) was much lower than that of PHES (77 dB).

Notably, the high-frequency power dynamics were absorbed when the gain offered by BESS increased beyond the cut-off
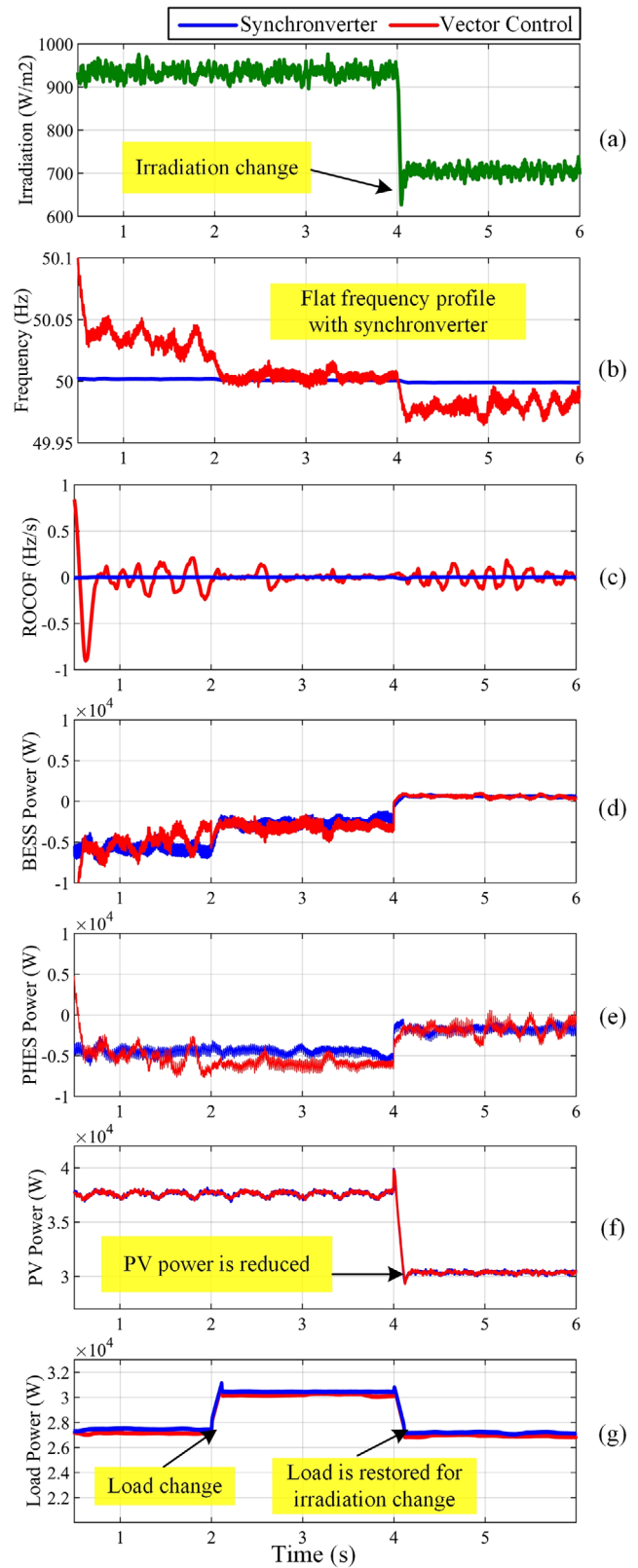
FIGURE 12 Performance analysis under load and irradiation changes while PHES is in pumping mode: (a) solar irradiation, (b) frequency, (c) ROCOF, (d) BESS power, (e) PHES power, (f) PV power, and (g) load power
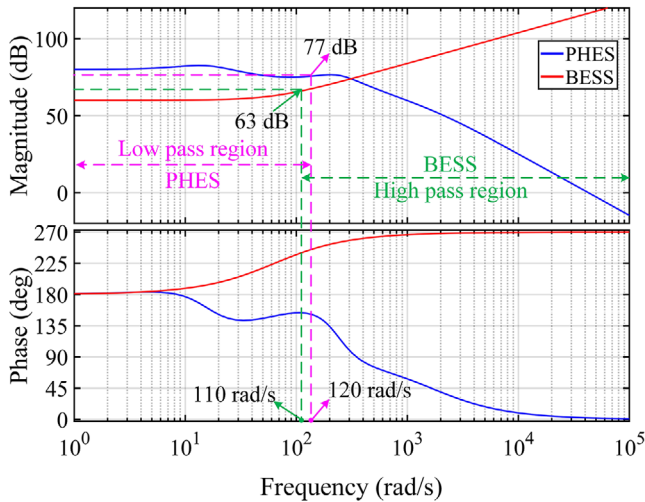
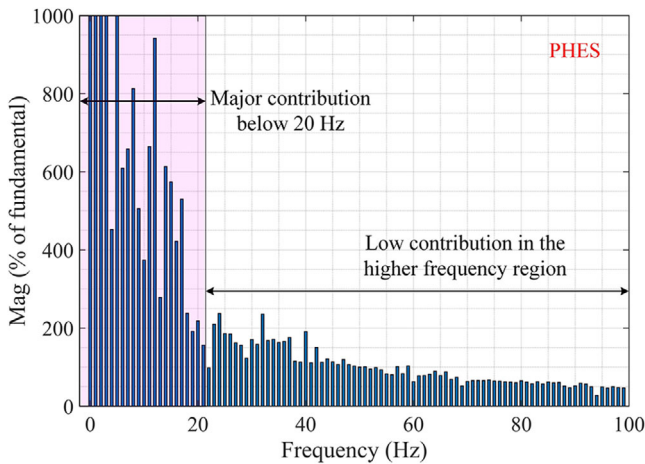**FIGURE 13** Closed-loop frequency response of PHES and BESS

FIGURE 14 Spectral decomposition of PHES power output

frequency of 110 rad/s (17.5 Hz). Furthermore, the spectral decomposition of power exchanged by BESS and PHES provided in-depth insight into the inherent behaviour of PHES. Hence, the power output of PHES and BESS were decomposed into frequency spectrums using the FFT analysis. The analysis corroborated with the frequency response characteristics that were presented above. PHES contributed to a major share below its cut-off frequency of 20 Hz (Figure 14). Meanwhile, the power share of BESS was present throughout the frequency spectrum, while its significant contribution was around 50 Hz (Figure 15). Hence, the FFT analysis also justified the inherent decoupling of power-sharing dynamics between PHES and BESS offered by the time constant of the hydraulic governor.

6 | CONCLUSION

The primary objective of this paper was to develop a frequency regulation strategy for an autonomous microgrid utilizing the
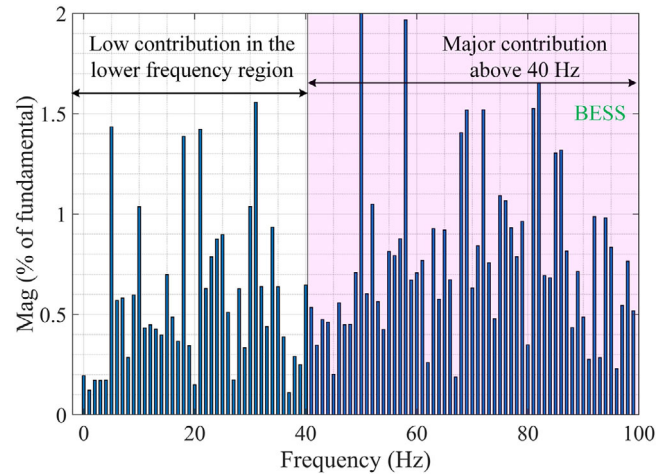

FIGURE 15 Spectral decomposition of BESS power output

PHES-BESS hybrid. Hence, the synchronverter control was proposed to control the PHES-BESS hybrid and emulate the virtual inertia in the microgrid. Firstly, the small-signal modelling of HESS with the proposed strategy was presented. The critical parameters affecting the frequency dynamics were utilized to assess the stability and the dynamic response of the system through small-signal analysis. Secondly, the performance metrics such as ROCOF and frequency nadir were employed to compare the proposed strategy against the vector control for the microgrid frequency regulation through time-domain simulations. Thus, this paper will serve as an initial work in the wake of hybridizing PHES with a faster acting ESS. The key conclusions of this paper are:

1. The system remained stable for a wide range of variations of critical parameters like virtual inertia and the hydraulic governor time constant.
2. The effects of varying virtual inertia of the synchronverter and the time constant of the hydraulic governor yielded similar responses. Hence, the governor time constant can be tuned to manipulate the dynamic response of the system to a certain degree.
3. The hydraulic governor exhibited the characteristics of a low pass filter, thus, contributed to the inherent decoupling of power-sharing dynamics between PHES and BESS.
4. The time-domain simulations revealed that the synchronverter control arrested the ROCOF within 0.5 Hz/s and frequency nadir/peak within 50 ± 1.5 Hz. Furthermore, the proposed strategy provided better frequency regulation of the microgrid compared to the classical vector control.

CONFLICT OF INTEREST
The authors declare no conflict of interest.

DATA AVAILABILITY STATEMENT

The data that support the findings of this study are available from the corresponding author upon reasonable request.

ORCID

Krishnakumar R. Vasudevan https://orcid.org/0000-0003-0831-1834

REFERENCES

1. Vasudevan, K.R., Ramachandaramurthy, V.K., Venugopal, G., Ekanayake, J.B., Tiong, S.K.: Variable speed pumped hydro storage: A review of converters, controls and energy management strategies. Renewable Sustainable Energy Rev. 135, 110156 (2021)
2. Pali, B.S., Vadhera, S.: An innovative continuous power generation system comprising of wind energy along with pumped-hydro storage and open well. IEEE Trans. Sustainable Energy 11(1), 145–153 (2020)
3. Musarrat, M.N., Islam, M.R., Muttaqi, K.M., Sutanto, D.: Enhanced frequency support from a PMSG-based wind energy conversion system integrated with a high temperature SMES in standalone power supply systems. IEEE Trans. Appl. Supercond. 29(2), 1–6 (2019)
4. Akram, U., Shah, R., Mithulananthan, N.: Hybrid energy stoarage system for frequency regulation in microgrids with source and load uncertainties. IET Gener. Transm. Distrib. 13(22), 5048–5057 (2019)
5. Said, S.M., Aly, M., Hartmann, B., Mohamed, E.A.: Coordinated fuzzy logic-based virtual inertia controller and frequency relay scheme for reliable operation of low-inertia power system. IET Renewable Power Gener. 15(6), 1286–1300 (2021)
6. Sanchez, F., Cayenne, J., Gonzalez-Longatt, F., Rueda, J.L.: Controller to enable the enhanced frequency response services from a multi-electrical energy storage system. IET Gener. Transm. Distrib. 13(2), 258–265 (2018)
7. Li, J., Xiong, R., Yang, Q., Liang, F., Zhang, M., Yuan, W.: Design/test of a hybrid energy storage system for primary frequency control using a dynamic droop method in an isolated microgrid power system. Appl. Energy 201, 257–269 (2017)
8. Shim, J.W., Cho, Y., Kim, S., Min, S.W., Hur, K., Member, S.: Synergistic control of SMES and battery energy storage for enabling dispatchability of renewable energy sources. IEEE Trans. Appl. Supercond. 23(2), 5701205 (2013)
9. Dreidy, M., Mokhlis, H., Mekhilef, S.: Inertia response and frequency control techniques for renewable energy sources: A review. Renewable Sustainable Energy Rev. 69, 144–155 (2017)
10. Sharma, R., Choudhary, D., Shiradkar, S., et al.: Who is willing to pay for solar lamps in rural India? A longitudinal study. Renewable Sustainable Energy Rev. 140, 110734 (2021)
11. Bevrani, H., Ise, T., Miura, Y.: Virtual synchronous generators: A survey and new perspectives. Int. J. Electr. Power Energy Syst. 54, 244–254 (2014)
12. Hesse, R., Turschner, D., Beck, H.-P.: Micro grid stabilization using the virtual synchronous machine (VISMA). Renewable Energy Power Qual. J. 1(07), 676–681 (2009)
13. Yan, W., Cheng, L., Yan, S., Gao, W., Gao, D.W.: Enabling and evaluation of inertial control for PMSG-WTG using synchronverter with multiple virtual rotating masses in microgrid. IEEE Trans. Sustainable Energy 11(2), 1078–1088 (2020)
14. Vasudevan, K.R., Ramachandaramurthy, V.K., Babu, T.S., Pouryekta, A.: Synchronverter: A comprehensive review of modifications, stability assessment, applications and future perspectives. IEEE Access 8, 131565–131589 (2020)
15. Michael, N.E., Hasan, S., Mishra, S.: Virtual inertia provision through data centre and electric vehicle for ancillary services support in microgrid. IET Renewable Power Gener. 14, (18), 3792–3801 (2020)
16. Høstmark, H., Amin, M.: Small-signal modeling and tuning of Synchronverter-based wind energy conversion systems. Int. Trans. Electr. Energy Syst. 31(5), e12848 (2021)
17. Mishra, S., Pullaguram, D., Buragappu, S.A., Ramasubramanian, D.: Single-phase synchronverter for a grid-connected roof top photovoltaic system. IET Renewable Power Gener. 10(8), 1187–1194 (2016)
18. Aouini, R., Marinescu, B., Ben Kilani, K., Elleuch, M.: Synchronverter-based emulation and control of HVDC transmission. IEEE Trans. Power Syst. 31(1), 278–286 (2016)
19. Liu, D., Zhong, Q., Wang, Y., Liu, G.: Modeling and control of a V2G charging station based on synchronverter technology. CSEE J. Power Energy Syst. 4(3), 326–338 (2018)
20. da Silva Junior, G.P., Barros, L.S., Barros, C.M.V.: Synchronverter coupled to a lithium-ion bank for grid frequency and voltage supports and controlled charge-discharge. Electr. Power Syst. Res. 197, 107352 (2021)
21. Gomes, L., Abrantes-Ferreira, A.J.G., Dias, R., Rolim, L.G.B.: Synchronverter-based STATCOM with voltage imbalance compensation functionality. IEEE Trans. Ind. Electron. 0046(c), 1–8 (2021)
22. Sarojini, R.K., Palanisamy, K., Sanjeevikumar, P., Nielsen, J.B.H.: Inertia emulation control technique based frequency control of grid-connected single-phase rooftop photovoltaic system with battery and supercapacitor. IET Renew. Power Gener. 14(7), 1156–1163 (2020)
23. Nakka, P.C., Mishra, M.K.: Droop characteristics based damping and inertia emulation of DC link in a hybrid microgrid. IET Renewable Power Gener. 14(6), 1044–1052 (2020)
24. Li, S., Li, Y., Chen, X., Li, T., Zhang, W.: A novel flexible power support control with voltage fluctuation suppression for islanded hybrid AC/DC microgrid involving distributed energy storage units. Int. J. Electr. Power Energy Syst. 123, 106265 (2020)
25. Working group on prime mover and energy supply: Hydraulic turbine and turbine control models for system dynamic studies. IEEE Trans. Power Syst. 7(1), 167–179 (no date)
26. Hu, J., Xu, Y., Cheng, K.W., Guerrero, J.M.: A model predictive control strategy of PV-Battery microgrid under variable power generations and load conditions. Appl. Energy 221, 195–203 (2018)
27. Energy Networks Association: Engineering Recommendation G59 Issue 3 Amendment 3. (2015) Energy Networks Association, UK, 2015. Accessed Sep. 16, 2019. [Online]. Available: https://www.nationalgrid.com/sites/default/files/documents/GC0079Annex3Option1G59proposals170731.pdf
28. Tamrakar, U., Shrestha, D., Maharjan, M., Bhattarai, B.P., Hansen, T.M., Tonkoski, R.: Virtual inertia: Current trends and future directions. Appl. Sci. 7(7), 1–29 (2017)
29. Gupta, P., Bhatia, R.S., Jain, D.K.: Active ROCOF relay for islanding detection. IEEE Trans. Power Delivery 32(1), 420–429 (2017)